ARTICLE

A sustainable porous composite material based on Loofah-Halloysite for gas adsorption and drug delivery

Received 00th January 2022,
Accepted 00th January 2022

DOI: 10.1039/x0xx00000x

Vincenzo Patamia,[a,†,*] Roberto Fiorenza,[b,†] Ilaria Brullo,[a] Massimo Zambito Marsala,[c] Stefano Andrea Balsamo,[b] Alfio Distefano,[d] Pio Maria Furneri,[d] Vincenzina Barbera,[c] Salvatore Scirè[b] and Antonio Rescifina[a,*]

The development of new advanced polymers has led researchers to look to nature to find new, high-performance, low-cost materials. This work aims to easily functionalize the fibers, made up of polysaccharides, of the loofah with halloysite through crosslinkers. Bio-composites have been extensively characterized using different techniques. The synthesized loofah-halloysite composites have improved CO_2 adsorption properties superior to both individual components and materials currently used in the industry. In particular, compared to the BEA and the MOR zeolites, it was measured an improvement in CO_2 capture of about 50% and 23%, respectively. Moreover, the composite investigated in this work showed superior CO_2 capture compared to other cellulose-based and sustainable materials. Furthermore, the presence of halloysite also increased the mechanical properties of the cellulosic polymer. The new cellulose composites have proved to be excellent candidates for the delivery of resveratrol, maintaining its anticancer activity. The results underline the synergistic effect of functionalization in increasing the adsorption properties compared to the starting materials and the possibility of using this eco-sustainable and low-cost porous system in various fields such as gas adsorption and drug administration.

Introduction

Currently, the environmental awareness of the global community boosted the interest of both academy and industry researchers in developing new advanced polymers which are both eco-friendly and able to exhibit the targeted properties for the required application. For this purpose, scientists often looked at nature, trying to mimic it to find eco-materials with high performance and low cost. Among these, the loofah sponge (L), a porous cellulose-based, light, and 3D structure material obtained from the matured dried fruit of *loofah cylindrica*,[1] has been used in many applications, such as cleaning products and insole materials,[1-3] pharmaceuticals,[4, 5] environmental engineering,[6, 7] biotechnology.[8] The high cellulose content of L has been exploited in the field of polymer composites,[9] and its high degree of lignification has great potential for its use in composite fibers.[10-14] Moreover, the highly porous structure provides excellent gas adsorption and facilitates effective light transmission,[15] allowing its use for gas adsorption and promising photocatalytic applications.[16] However, L must be coupled with inorganic materials to provide better physical, chemical, and mechanical properties to expand its applicability.[16]

In this work, we functionalized the L fibers with halloysite (H), a natural clay mineral of the kaolin group,[17] to improve the loofah's adsorption performance and mechanical resistance. This approach was used in the literature where the combination of the properties of H, as a natural material, with a unique tubular nanostructure, large aspect ratio, biocompatibility, and high mechanical strength, improved the properties of polymer composites.[18]

This is the first attempt to prepare and apply this L-H as a bio-composite.[19, 20]

H has a 1D tubular structure in the range of mesopores (2–50 nm) and macropores (>50 nm).[21] This more significant porosity with respect to other known synthetic porous materials, such as carbon nanotubes (CNT),[22] qualifies H for loading large molecules such as drugs and enzymes.[23]Moreover, its peculiar tubular aluminosilicate structure enables H to be variously functionalized (external, internal, and interlayer surface), thus making it highly versatile.[17, 24] Finally, H has been proved to show low toxicity.[25]

Specifically, in this work, we used different crosslinkers for the L functionalization with H. The new cellulosic composites were characterized by several techniques (Fourier-transform infrared

[a] *Department of Drug and Health Sciences, University of Catania, V.le A. Doria 6, 95125 Catania, Italy. E-mail: vincenzo.patamia@unict.it , arescifina@unict.it*
[b] *Department of Chemical Sciences, University of Catania, V.le A. Doria 6, 95125 Catania, Italy.*
[c] *Department of Chemistry, Materials and Chemical Engineering "G. Natta", Politecnico di Milano, Via Mancinelli 7, Milano, 20131, Italy*
[d] *Department of Biomedical and Biotechnological Sciences (BIOMETEC), University of Catania, Via Santa Sofia, 97, 95123 Catania, Italy.*
† These authors contributed equally.
Electronic Supplementary Information (ESI) available: Experimental Procedures, Characterizations, CO_2 adsorption and CO_2-TPD measurements, Biological assay. See DOI: 10.1039/x0xx00000x

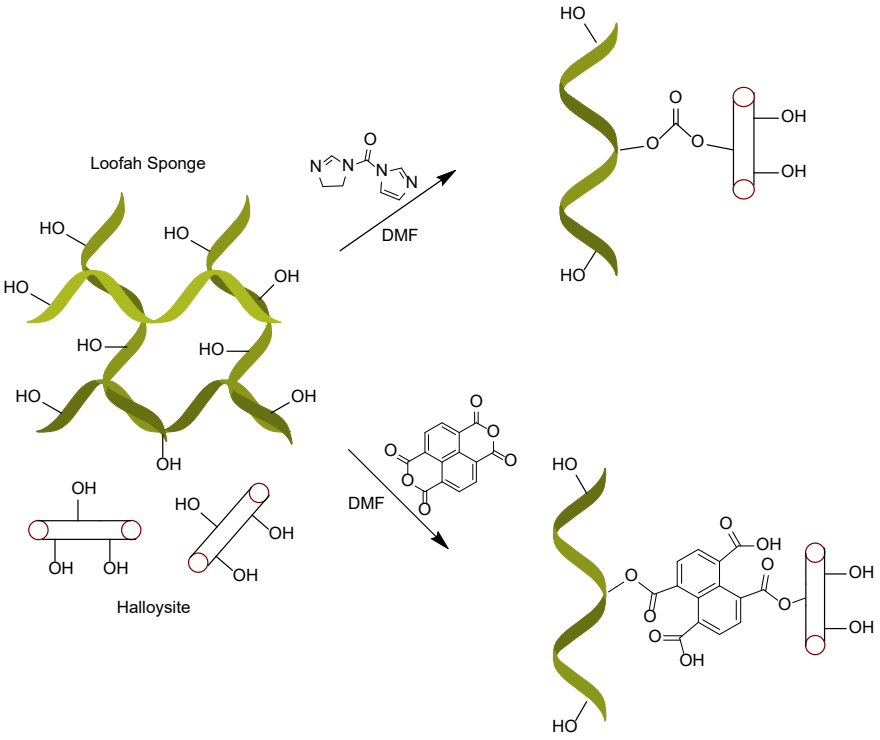

Fig. 1 Synthesis of the loofah-halloysite composite.

spectroscopy, Thermogravimetric analysis, High-Resolution Transmission Electron Microscopy, and Tensile test). These composites were applied for the carbon dioxide capture, showing superior adsorption capacities to the single components, L and H, and to zeolites, which are currently used in industry. Furthermore, they also proved to be candidates for the adsorption/delivery of resveratrol, a natural phenolic compound found in grape skin and other plants, with many beneficial effects on human health, as an antioxidant, antitumor, neuroprotective, and antiviral activities.[26-28]
The results of this study underline that the functionalization of polysaccharide fibers with H gives rise to a synergistic effect enhancing the adsorption properties compared to the starting materials, thus pointing to the possibility of using this new low-cost, eco-friendly, and biocompatible composite in various fields such as gas adsorption and drug delivery.

Results and discussion

Materials preparation

The polypores material was synthesized using loofah (L) and halloysite (H) by exploiting the surface hydroxyl groups to bind them via a crosslinker. The crosslinkers used were: 1,1'-carbonyldiimidazole (C) and 1,4,5,8-naphthalenetetracarboxylic dianhydride (N), both of which have often been used for the synthesis of different materials such as cyclodextrin nanosponges (Fig. 1).[29, 30] An L:H ratio of 1:5 w/w was used, and the molar ratios of the crosslinkers were varied with respect to H. In particular, ratios of 2, 10, and 20 equivalents were used for each crosslinker. Composites prepared with C will be named with the acronym LHCx and composites prepared with 1,4,5,8-Naphthalenetetracarboxylic dianhydride will be named with the acronym LHNx, where x indicates the crosslinker equivalents with respect to H (Table 1).

Pristine materials and composites characterization

Pristine loofah (L), halloysite (H), and LH composites were characterized by employing thermogravimetric analysis (TGA), Fourier-transform infrared spectroscopy (FT-IR), Scanning Electron Microscopy (SEM), transmission electron microscopy (TEM), and high-resolution transmission electron microscopy (HR-TEM). The amount of H in both LHCx and LHNx composites was checked through TGA. The thermographs of all samples are reported as supplementary material (Fig. S2a,b). Mass losses (mass %) of composites and pristine materials are reported in Table 2. The decomposition profile of L shows three main steps, at the following temperatures: below 150 °C, between 150 °C and 380 °C, and above 380 °C. The mass loss at T < 150 °C could be reasonably attributed to the release of water molecules on the surface.

Table 1 Reaction conditions for the synthesis of LHCx and LHNx compositesa

L:H ratio 1:5 w/w				
Time h	H:C ratio (eq.)	Composite name	H:N ratio (eq.)	Composite name
3	1:2	LHC2	1:2	LHN2
12	1:10	LHC10	1:10	LHN10
24	1:20	LHC20	1:20	LHN20

[a]All reactions were carried out in DMF at 80 °C.

Table 2 Mass losses (mass %) for pristine L, H, LHCx, and LHNx composites, from TGA analysis[a]

Sample	Mass loss (%)			Residue (%)
	T < 150 °C	150 °C < T < 380 °C	380 °C < T < 700 °C	T > 700 °C
Halloysite	1.2	1.8	11.2	85.8
Loofah	3.0	67.0	29.0	1.0
LHC2	5.5	64.5	26.5	3.5
LHC10	4.0	66.0	26.0	4.0
LHC20	4.0	66.5	24.5	5.0
LHN2	3.0	66.5	26.0	4.5
LHN10	3.0	66.0	24.0	7.0
LHN20	3.0	67.0	20.0	10.0

[a]Tests were conducted with a temperature ramp of 10 °C/min from 25 °C to 900 °C in an inert nitrogen atmosphere, followed by 15 min isotherm at 900 °C in air flux.

Table 3 Loading of H (%) in LHCx and LHNx composites calculated from TGA data

Sample	H loading (%)	Sample	H loading (%)[a]
LHC2	2.5	LHN2	3.5
LHC10	3.0	LHN10	6.0
LHC20	4.0	LHN20	9.0

[a]Calculated by applying Equation 1.

The mass loss from 150 °C to 380 °C is attributed to the polysaccharide component (hemicellulose and cellulose). The mass loss at T > 380 °C is due to the decomposition of the lignin component.[31]

The thermal profile of H showed a mass loss in the range of temperature of 25–150 °C related to the release of water molecules on the surface, while the mass loss at T > 400 °C is due to the so-called bound water (structural water) loss and the dihydroxylation process.[32]

At T 150 °C, all the investigated composites showed a mass loss attributed to the release of water, while at high temperatures, mass losses are the result of L decomposition.

For all LH samples, the residual amount was also reported and used to indicate the actual amount of H. Based on these residue values, the theoretical and experimental loading of H (%) were compared.[33] The experimental H loading % of LHCx and LHNx composites, calculated by applying Equation 1, is reported in Table 3.

$$H\ loading\ \% = (LH\ residue\ \% - L\ residue\ \%) \qquad (1)$$

Where, LH residue and L residue are the residual amounts at T > 700 °C for LH composites and Loofah, respectively, as reported in Table 2.

FT-IR was used to study the nature of functional chemical groups. Pristine materials and LH composites were characterized by employing attenuated total reflectance Fourier transform infrared spectroscopy (ATR-FTIR). Functional groups were detected by analyzing the samples on a zinc selenide crystal (ZnSe) (Fig. 2a,b).

In the spectrum of L, bands due to the lignocellulosic structure can be detected: (i) the broad peak centered at 3400 cm^{-1} is related to the O–H stretching of the alcohol groups of cellulose; (ii) the band due to CH_2 stretching are at 2920 cm^{-1}; (iii) the broadband at 1695 cm^{-1} is the result of the superimposition of C=O stretching coming from either the hemicellulose component or the lignin part; (iv) the C–O–C symmetric stretching at 1100 cm^{-1}; (v) the C–OH stretching vibration at 1055–1060 cm^{-1}; (vi) the band at 1430 cm^{-1} is attributed to the CH_2 bending of cellulose; (vii) bands at 1370 cm^{-1} and 1320 cm^{-1} are associated with the alcohol groups of the cellulose.[34]

In the spectrum of H, bands related to OH groups are evident: the peak at 910 cm^{-1} is ascribable to the Al–O–OH vibration, while the bands at 3710 and 3630 cm^{-1} are attributed to the stretching vibration of the inner-surface Al–OH groups. A strong O–Si–O peak is observed at around 1150 cm^{-1}, and the peaks at 770 and 745 cm^{-1} are assigned to the stretching mode of apical Si–O.[35]

In the spectra of all LH composites (Fig. 2A,B), bands related to the starting materials are clearly observed along with other features due to the chemicals used to generate the bond between H and L. In LHCx samples, a new weak signal appears at 1747 cm^{-1}, related to the C=O stretching of the carbonate bridge group.

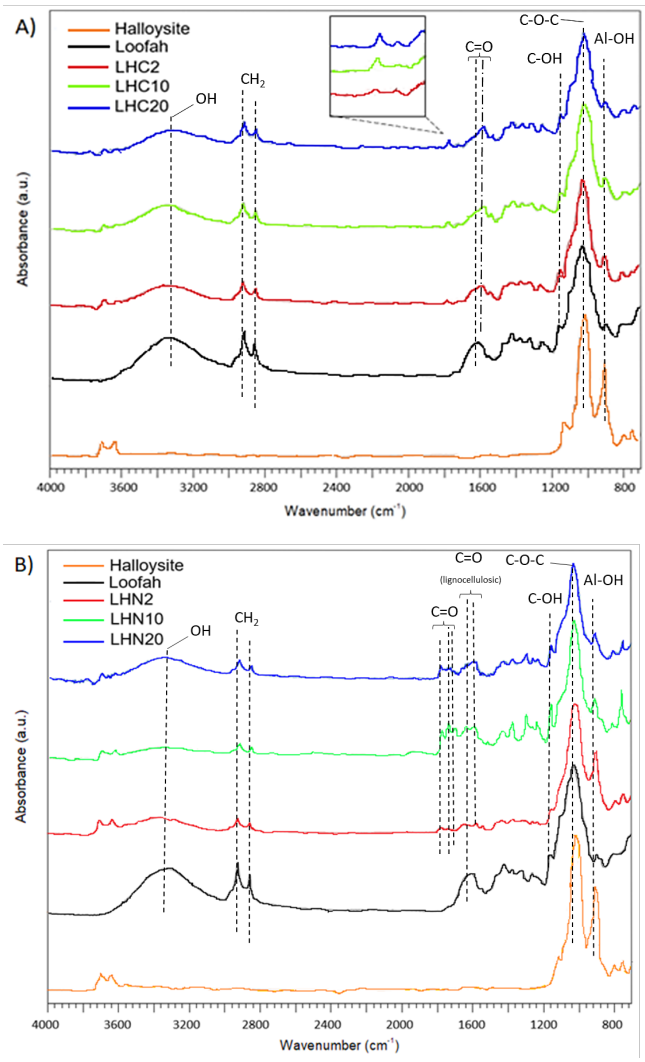

Fig. 2 ATR-FTIR spectra of H (orange line), L (black line) and LH composites: a) LHC2 (red line), LHC10 (green line) and LHC20 (blue line); b) LHN2 (red line), LHN10 (green line) and LHN20 (blue line). The magnification in the 1600–1700 cm^{-1} region is in the insert of Figure 2A.

This new band, along with other new features, demonstrates that the functionalization procedure with C was successful. These new features, linked to the chemical alteration of the lignin component, seem to suggest that the chemical bond has been formed with this part: the deformation of the macro band at 1695 cm^{-1} could show the possibility that the new bond was also formed with the OH (glycerol moiety) of the lignin. The presence of the new functional group or the loss of carbonyl functional groups on the lignin structure due to the thermal treatment could be responsible for these shape changes.

In LHNx samples, a new series of signals appear in the range between 1800–1598 cm^{-1}: the band at 1610 cm^{-1} is related to C=O stretching vibration of CO_2H, whereas the band at 1790 cm^{-1} corresponds to the C=O stretching vibration of hydrogen-bonded esters. As already underlined in the case of the previous functionalization (LHC samples), some changes in the structure of the band at 1695 cm^{-1} are clearly visible. The formation of a bond with the alcoholic portion of the lignin and the loss of carbonyl functional groups are hypothesized for this kind of functionalization.

A Morphological investigation of L, H, and LH composites was performed through TEM and HR-TEM. The LHC10 sample had been selected and analyzed to check if the morphology had been maintained after the functionalization procedure. The latter was chosen since it allowed, unlike all the other samples, the deposition of an adequate amount of the composite, enabling statistical analysis of the material morphology.

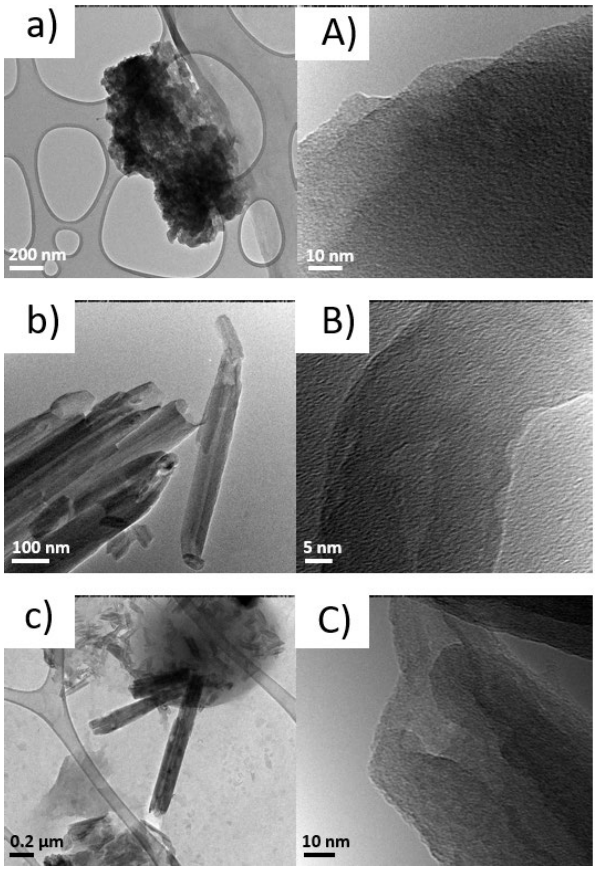

Fig. 3 Micrographs of L (a, A), H (b, B), and LHC10 (c, C), after mild sonication for 5 min. Bright-field TEM micrographs at low magnification (a–c). HR-TEM micrographs (A–C).

Acetone suspensions of L, H, and LH composites, with 1 mg/mL as the concentration, were sonicated for 5 minutes using an ultrasonic bath.

The suspensions were then analyzed, and micrographs were taken at lower and higher magnification (Fig. 3).

The micrograph at lower magnification in Fig. 3a reveals that the morphology of L seems to be characterized by a highly disordered texture. The statistical analysis performed on many micrographs underlines the high purity of this lignocellulosic material. HR-TEM image (Fig. 3A) suggests that the pristine L could have a light graphitized layer on the surface.

Morphologies of H nanotubes and LHC10 have been checked, and micrographs are in Fig. 3. The micrographs taken at high magnification in Fig. 3B,C show a regular nanotube skeleton in both samples. The inspection of such images allowed us to detect the lengths of H tubules (0.5 to > 10 µm) and a diameter in the range of 50 to 110 nm. The micrographs at low magnification reveal a different degree of aggregation for the pristine (Fig. 3b) and functionalized (Fig. 3c) halloysite nanotubes: bundles of oriented and aligned nanotubes are clearly visible in the former Fig. 3b, whereas the more disordered distribution and the presence of L on the nanotubes is appreciable in the latter one (Fig. 3c). It appears that the functionalization procedure can lead to an appreciable nanotubes-L interaction. Another essential information from the HR-TEM investigation is that the sonication and functionalization processes did not modify the nanotubes dimensions.

Tensile tests were performed on starting material and LH composites. The samples have been pulled with the method reported in Table S1 (see Supporting Information).

In Fig. 4, it is observed that the concentration of crosslinker and thus of H influenced the mechanical properties of LH composites compared to L. Specifically, both LHNx and LHCx showed an ultimate elongation with H: C and H: N ratios equal to 1:10. The further incorporation of H decreased the elongation at break. This reduction can be explained by considering H/L interactions that decrease the slide of L fibers.

When the stored energy of the composites during the tensile experiments was evaluated, the same effect was noticed. In detail, untreated L showed stored energy of 1543 kJ m^{-3}, and this value raised significantly to LHN10 and LHC10, with stored energy equal to 8556 kJ m^{-3} and 7586 kJ m^{-3}. LHC20 presented the lowest stored energy (1642 kJ m^{-3}). These results are in line with the data of elongation at break.

SEM images of L and LHNx composites are shown in Fig. S3. From Fig. S3a, it is observed that the surface of the fibers is tightly banded; the interior of the L fiber had a porous structure with the diameter of the macropores of 12–20 microns. This is in accordance with the literature; indeed, the L-based materials are notably characterized by the presence of macropores.[36, 37]

It is worth noting that the material intrinsic porosity cannot be determined with the N_2 adsorption-desorption measurements due to large macropores (as described before) and the peculiar shape of the loofah (L) fibers.

Fig. S3b,c represent the SEM images of L/H composites treated with dianhydride. A better distribution of the nanotubes on the

L surface (red arrows) demonstrates an increase in the amount of H. This behavior was visible when LHN2 and LHN20 composites were compared.

The dimensions of the nanotubes are consistent with those detected by analyzing micrographs obtained from transition electron microscopy (0.5–2.0 μm). The increased distribution of the nanotubes appears to agree with the results of the tensile tests. The LHC series show similar morphology.

CO_2 adsorption and CO_2-TPD measurements

The CO_2 adsorption capacity of the investigated materials at room temperature and atmospheric pressure is illustrated in Fig. 5 (the corresponding breakthrough curves are reported in the Supporting Information Fig. S4). For the sake of comparison, two zeolites were used, a BEA zeolite (CP 811-300, SiO_2/Al_2O_3 = 300, BET surface area 280 m^2/g) and a MOR zeolite (CBV 21 ammonium form, SiO_2/Al_2O_3 = 20, BET surface area 500 m^2/g). These zeolites are widely used as CO_2 and gases sorbents.[38-41] Furthermore, Fig. 5 displays the amount of CO_2 adsorbed on the grounded mixed sample of L and H coded as LHM (*i.e.*, without the addition of crosslinkers). The bare L showed the lowest CO_2 adsorption capacity (q = 8.9), whereas the pure H (q = 143) performance was similar to that of the MOR zeolite. The addition of the crosslinkers to the H and L allowed to increase the amount of adsorbed CO_2 with the sample LHC10 that exhibited the highest value (q = 162.8).

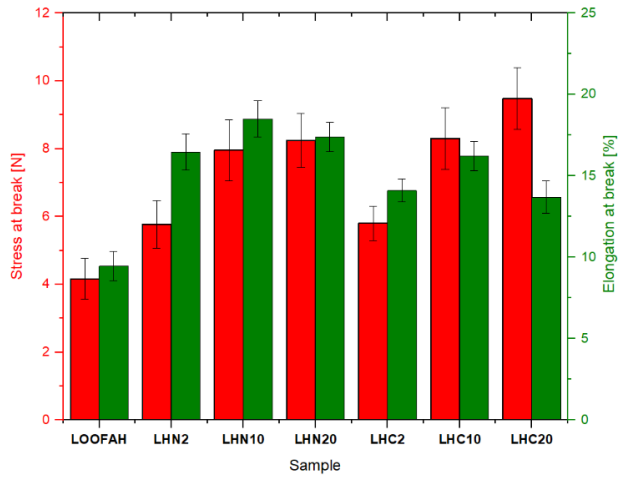

Fig. 4 Effect of H content on tensile properties of HL composites.

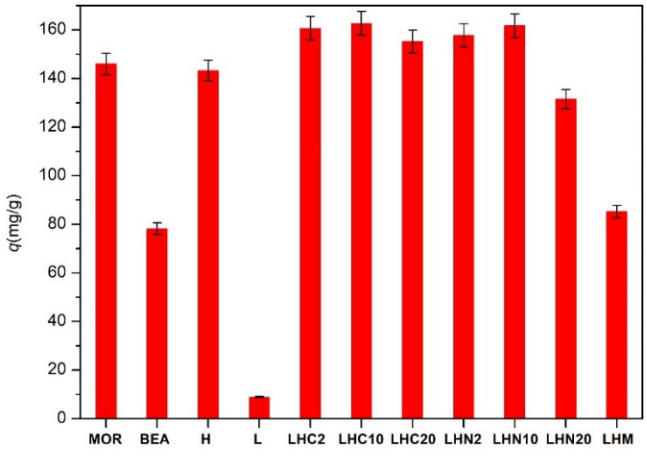

Fig. 5 The CO_2 adsorption capacity of the investigated samples.

A lower amount of crosslinker C (LHC2) did not alter the adsorption capacity of the composites, whereas a slight decrease was verified in the case of the crosslinker N (LHN2, q = 157.9 and LHN10, q = 161.8). A further increase of both C and N crosslinkers amounts led to an additional loss in CO_2 adsorption, more relevant for the LHN20 (q = 131.5) than the LHC20 sample (q = 155.2). By adding naphthalene groups, they were probably induced hindrance effects that did not favor the adsorption of CO_2. The CO_2 adsorption trend can be rationalized considering the loading of H reported in Table 3. Indeed, after a definite H loading, the synergistic effect between the H and L was progressively lower, following a "volcano" trend. In particular, for the crosslinker C the best loading was 2.5–3.0% of H, whereas, for the N crosslinker, the maximum was between 3.5 and 6.0% of H. Interestingly, the combination of L and H especially promoted by the crosslinker C with a definite amount, allowed to exploit a holistic effect. Indeed, the bare L and H performance sum gave a q value of 151.9, lower than the best composite LHC10 (162.8), where the amount of loaded H on L is only the 3.0% (Table 3), significantly lower than the pure H. This pointed out that only the strong interaction between the two components of the hybrid composite mediated by the crosslinker led to a synergistic effect that favored the CO_2 adsorption. It is important to highlight that this synergy allowed to obtain a superior performance of CO_2 adsorption compared to other cellulosic and sustainable-based materials.[42-44]

Five consecutive runs of CO_2 adsorption-desorption measurements were carried out to determine the reusability properties of LHC2. Based on the CO_2-TPD profile of LHC2 (Fig. S5), after the adsorption of CO_2 and the surface saturation, the CO_2 flow was stopped, and the sample was heated from room temperature to 180 °C (the CO_2 desorption peak was at 171 °C). The composite was cooled under He flow, and the CO_2 flow was turned on to favor its adsorption to perform the subsequent run.

From Fig. 6, it is possible to note that the adsorption capacity of the LHC2 composite started to become lower from the third run, reaching in the fifth run a q value of 132.8. This behavior can be reasonably ascribed to the folding of the L favored to the consecutive run of heating and cooling.[45] Although the degradation of the composite started at 230 °C, as stated by the TGA measurements (Fig. S2a,b), the heating at a temperature near to the initial thermal degradation of the composite (180 °C, necessary for the desorption of CO_2) can create L aggregates in the structure of the hybrid material that harmed the adsorption properties. However, comparing Fig. 5 and 6, it is essential to highlight that after the fifth run, the performance of the LHC2 material was better than BEA zeolite and LHM samples.

The kinetic tests of the CO_2 adsorption were carried out with the same sample (LHC2) and in comparison with the bare components of the composite (H and L) (Fig. 7, Table 4).

Based on the literature[46, 47] the experimental data were fitted with the Linear Driving Force (LDF) and the Pseudo-Second Order (PSO) models. These kinetic models are widely used to describe the CO_2 adsorption kinetics.[46-48] The LDF model

presumes that the adsorption rate is proportional to the number of the free surface sites suitable for the adsorption. The main driving force of the process is determined by the difference between the q at equilibrium and the q at the time t, whereas all the resistances due to the mass transfer are gathered by the kinetic parameter k_t as global resistance to the diffusion, following the equation (in the linear form):

$$\ln(q_e - q_t) = \ln q_e - k_t\, t$$

where q_t and q_e were the amounts of CO_2 absorbed per unit mass of the sample at time t and at the equilibrium, respectively.

Differently, the PSO model considers that the adsorption process is dominated by the chemisorption between the adsorbate and the adsorbent surface, following the equation:

$$\frac{t}{q_t} = \frac{1}{k_s q_e^2} + \frac{t}{q_e}$$

where k_s is the adsorption rate constant.

From the data reported in Fig. 7 and Table 4 it is evident that the PSO model well fits with the experimental data (R^2 = 0.99 for all the examined samples), pointing to the chemisorption of CO_2 as the driving force of the process. The CO_2-TPD measurements also confirmed this hypothesis. Indeed, the CO_2 desorption peak of the LHC2 composite was at 171 °C (Fig. S5) in the temperature zone of basic sites with medium strength (from 150 to 475 °C).[49] On the contrary, the LDF model, did not fit with the experimental data of all the samples since linearity was verifiable only at the begging of the adsorption process (from 5 to 15 min). Furthermore, the experimental values of q_e were very similar to those determined with the PSO model (Table 4). The LHC2 confirmed its high capacity of CO_2 capture (highest q_e value), followed by the bare H and the unmodified L. This latter sample showed the highest value of the k_s of the PSO model. Indeed, due to the poor interaction between the L and the carbon dioxide, the adsorption was fast and the quantity of adsorbed CO_2 low. On the contrary, in the LHC2 sample, the loading of H was low (2.5%, determined by TGA, Table 3); this was sufficient to establish a synergistic interaction with the L. The H was efficiently deposited and dispersed on the L; in fact, it can expose all the surface sites suitable for the CO_2 adsorption, thus favoring the CO_2 chemisorption. Therefore, the obtained composite showed better performance than the single H sample. It allowed overcoming the drawbacks of the pure L, whose very large macropores did not permit to capture CO_2 molecules efficiently.

Further confirmation of the strong interaction between the new hybrid material and carbon dioxide was verified by FTIR investigation. In particular, it was possible to deduce from Fig. 8 that after 24 hours of the adsorption of CO_2, the samples LHC2 and LHN2 showed the typical stretching of carbon dioxide at 2352 cm^{-1}.[50, 51] Interestingly, even after 48 hours, both samples showed the same band (Fig. 9).

Drug loading

To exploit the current uses of L[52] and H[53] in the cosmetic field, we have performed the loading and release experiments of

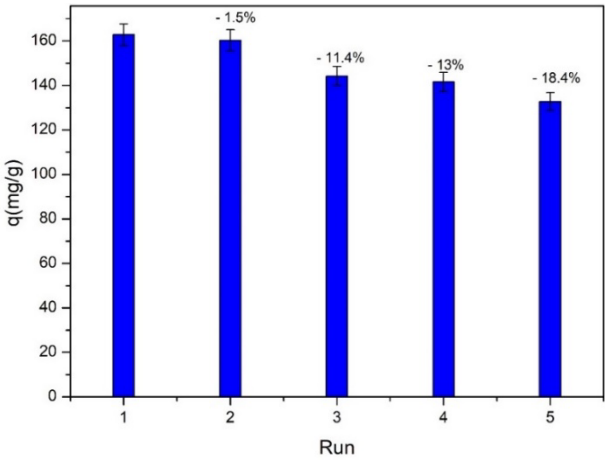

Fig. 6 The adsorption capacity of LHC2 composite after five consecutive runs of CO_2 adsorption-desorption.

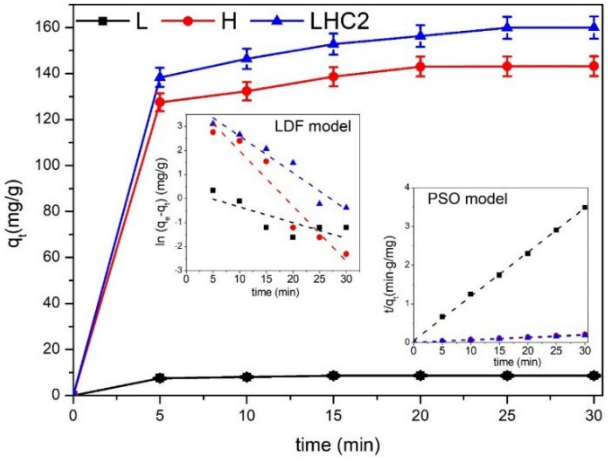

Fig. 7 Kinetic of the CO_2 adsorption on the bare loofah, halloysite, and on the LHC2 samples. The experimental data (points) and the fit (dashed lines) with the LDF and the PSO models are shown in the insets.

resveratrol, which has anti-aging properties,[54] for a possible topical application of this bio composite.

Resveratrol charge on LHC2 composite was carried on at different weight ratio: 1:10, 1:50, 1:100 and 1:1000 (drug: LHC2 w/w, Fig. S6). Briefly, 30 mg/L resveratrol solution was prepared, and the correct amount of LHC2 was suspended and kept under stirring for 1 h in the dark. Then, the suspension was centrifuged to separate the L materials from the uncharged drug.

The Drug Loading Capacity (DLC) and Encapsulation Efficiency (EE) were evaluated using the spectrophotometric UV-vis method at 303 nm with a JASCO V-730 instrument.

A calibration curve reporting the value of the absorbance in function of the resveratrol concentration was previously built (Fig. S8). To remain in the Lambert-Beer law regime, every solution was diluted to 5.4 mg/L before each analysis. The DLC and the EE were evaluated following Equations 2 and 3, respectively:[55, 56]

$$DLC = \frac{loaded\ drug\ amount}{total\ loofah\ amount} \qquad (2)$$

Table 4 Kinetic model parameters of the Linear Driving Force (LDF) and Pseudo-Second Order (PSO) for the CO_2 adsorption onto the bare Loofah, Halloysite, and LHC2 samples

Sample	q_e (mg/g) experimental	LDF model	PSO model
L	8.9	q_e (mg/g) = 3.4 k_t (min^{-1}) = 0.15 R^2 = 0.942 (first 3 points)	q_e (mg/g) = 8.7 k_s (min^{-1}) = 0.258 R^2 = 0.998
H	143.3	q_e (mg/g) = 71.8 k_t (min^{-1}) = 0.23 R^2 = 0.930	q_e (mg/g) = 144.9 k_s (min^{-1}) = 0.014 R^2 = 0.999
LHC2	161.0	q_e (mg/g) = 28.72 k_t (min^{-1}) = 0.15 R^2 = 0.946	q_e (mg/g) =161.3 k_s (min^{-1}) = 0.010 R^2 = 0.999

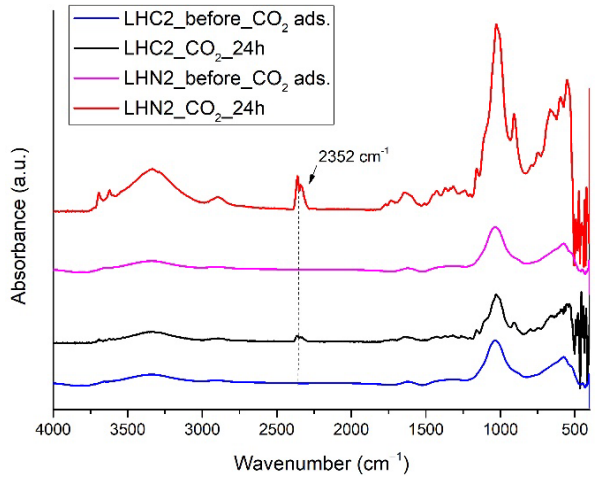

Fig. 8 FTIR spectra of LHN2 and LHC2 before and after 24 h of CO_2 adsorption.

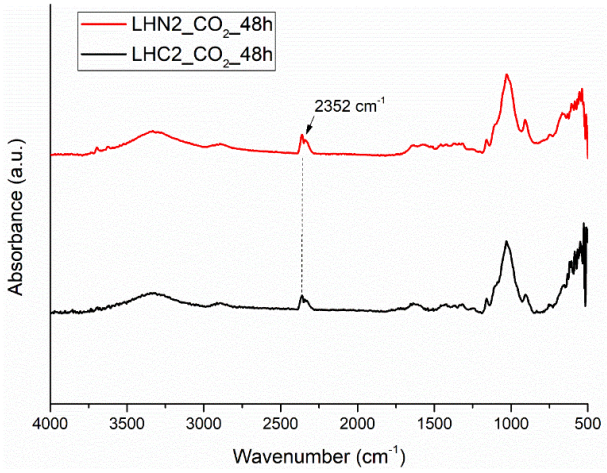

Fig. 9 FTIR spectra of LHN2 and LHC2 after 48 h of CO_2 adsorption.

$$EE = \frac{loaded\ drug\ amount}{total\ drug\ amount} \qquad (3)$$

From Fig. 10, it is possible to note that the highest EE was obtained with the highest quantity of adsorbent, as expected. However, it is more suitable for our purpose to evaluate the DLC that is optimized with a 1:10 drug-adsorbent ratio. The results obtained are in line with the data reported in the literature for the delivery of resveratrol.[57] The resveratrol loading capacity measurements were also performed on the individual starting materials (Fig. S7). The latter showed no-significant load capacity (around 2%), which underlines, as in the case of CO_2 adsorption, the synergistic effect of the functionalization of the L with the H. This highlights the key rule of crosslinker C that allows exploiting the macroporosity of L combined with the nanotubular H structure.

Finally, Fig. 11 illustrates the release kinetic of the resveratrol from the LHC2 sample when the 1:100 resveratrol/LHC2 loading ratio was chosen to evaluate the % of drug release in the most proper way. This was calculated considering the UV-vis calibration curve, correlating the measured absorbance with the concentration of resveratrol at each time point.

In accordance with the literature,[58, 59] the release kinetic was characterized by a first step (until 5 h) in which the drug release was very fast (about the 40% of release). Then, it was followed by a prolonged slower phase, reaching the 50% after 20 h and then 60% after 40 h. The rapid release in the initial time is due to the fast dissolution of the drug stored in the clay nanotubes and the H/L pockets, whereas the remaining drug molecules were released through a slow desorption process from the sample surface that is also influenced by the diffusion.[58] A similar resveratrol release kinetic was reported for other H-based materials or lipid nanoparticles.[58, 59]

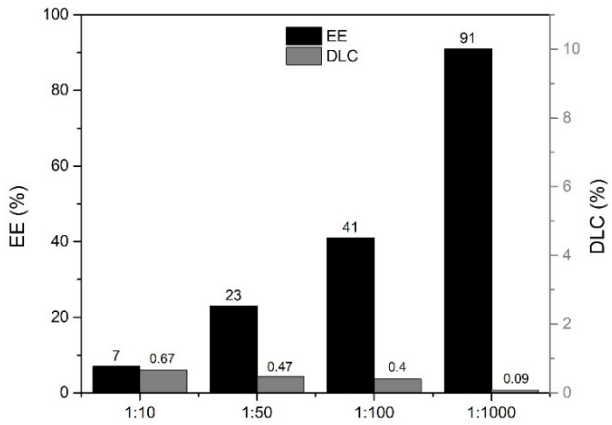

Fig. 10 Encapsulation Efficiency (EE) and Drug loading capacity (DLC) of resveratrol on LHC2 composite.

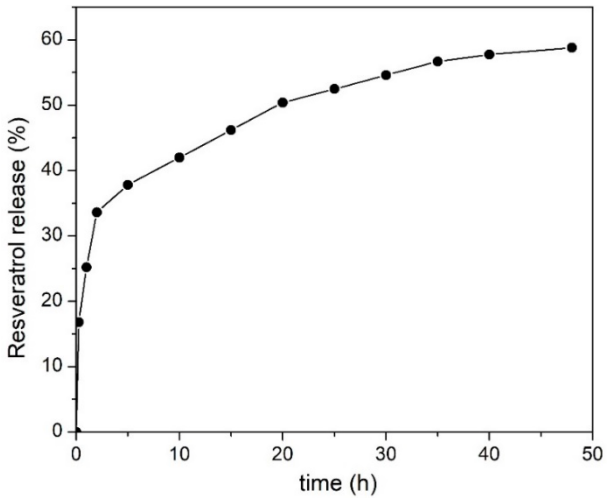

Fig. 11 Resveratrol release from the LHC2 sample.

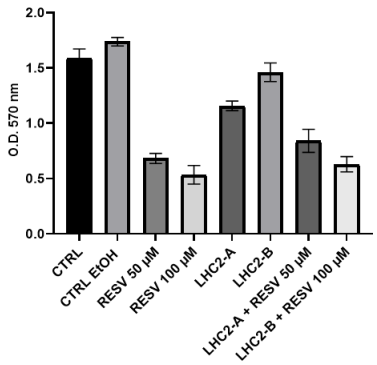

Fig. 12 Biological activities of resveratrol alone and associated with LHC2 (1:10 w/w; LHC2-A = 1.63 mg/mL, and LHC2-B = 3.26 mg/mL) against HTC 116 cell lines at 72 h.

Biological studies

To test the cytotoxicity of the new biomaterial, as it is, and in the presence of loaded resveratrol. It was performed an in vitro biological assay on HTC-116 colon cancer cells proliferation by the MTT method. Fig. 12 shows the biological activity of resveratrol alone and in association with LHC2 against HTC-116 cells. Our data show a specific inhibitory activity of cell viability of resveratrol alone and in association with LHC2. In particular, the activity of resveratrol alone is equal to a maximum percentage of reduction of 69.3% and strongly dependent on the type of control used for comparison (66.4–57.1% versus the control without ethanol and 69.3–60.8% versus the control with ethanol). In fact, as previously demonstrated,[60] ethanol, the solvent used for better solubilizing the resveratrol, has shown a positive effect on cell viability equal to 9.5% compared to the untreated control.

The cytotoxic activity of LHC2 (27.1–7.9% versus the control without ethanol and 33.4–15.9% versus the control with ethanol) is lower and inversely proportional to the dose used; this is probably due to a saturation effect rather than to a specific mechanism, given its non-solubility. In the association with resveratrol, this phenomenon is evidently canceled by its specific and powerful inhibitory action; however, there is a slight decrease in intrinsic activity compared to the data obtained from resveratrol alone (60.4–47.1% versus the control without ethanol and 63.8–51.7% versus ethanol control). The statistical analyses have been reported in Figures S9–11.

Based on these results, we can conclude that resveratrol confirmed its potent inhibitory activity. Interestingly, the association with the LHC2 vehicle did not significantly lose its intrinsic activity.

Conclusions

In summary, to tackle the current adsorption problems of greenhouse gases, such as CO_2, and the possibility of using eco-friendly materials for drug delivery, the development of new low-cost, easy-to-prepare, and environmentally sustainable materials could help to solve these problems. We have developed a straightforward and rapid synthetic methodology to synthesize a new polymer composite, ecological and reusable material starting from cheap materials such as L and H. Considering the low amount of H bound to L, the composites showed a significantly greater ability to absorb and retain carbon dioxide than starting materials. This underlines the synergistic effect of the two materials, which also possess a greater adsorption capacity than the BEA and MOR zeolites, which are currently used in the industrial field for gas adsorption and require more prolonged and more expensive synthetic processes. Nevertheless, it is essential to underline that the composite investigated in this work showed superior performance compared to other cellulose-based and sustainable materials. In addition, the presence of halloysite improves the mechanical properties of the loofah fibers.

Moreover, the synergistic effect of the composite is evident in the greater carrying capacity of resveratrol compared to individual materials. Finally, the association with the LHC2 vehicle did not significantly affect the inhibitory activity of resveratrol against HCT-116 tumor cell lines. This study opens another way towards developing composite, organic-inorganic materials, applicable in multiple fields and at the same time eco-sustainable and economical.

Conflicts of interest

There are no conflicts to declare.

Acknowledgements

We acknowledge Mr. Mario Rapisarda for his fruitful suggestions.

Notes and references

1. Y. X. Chen, K. T. Zhang, F. C. Yuan, T. T. Zhang, B. B. Weng, S. S. Wu, A. Y. Huang, N. Su and Y. Guo, Properties of Two-Variety Natural Luffa Sponge Columns as Potential Mattress Filling Materials, *Materials*, 2018, **11**.
2. J. H. Shen, Y. M. Xie, X. D. Huang, S. W. Zhou and D. Ruan, Mechanical properties of luffa sponge, *J Mech Behav Biomed*, 2012, **15**, 141-152.
3. E. Alvarado-Gomez, J. I. Tapia and A. Encinas, A sustainable hydrophobic luffa sponge for efficient removal of oils from water, *Sustain Mater Techno*, 2021, **28**.
4. K. S. Choi, Y. H. Kim, S. O. Kim, K. O. Shin and K. H. Chung, Effect of intake of sponge gourd (Luffa cylindrica) seed oil and Yukdomok (Chionanthus retusa L.) seed oil on lipid levels of blood and organs of a mice, *Food Sci Biotechnol*, 2013, **22**, 757-763.
5. M. R. Islam, H. Nishida and G. Funatsu, Complete Amino-Acid-Sequence of Luffin-a, a Ribosome-Inactivating Protein from the Seeds of Sponge Gourd (Luffa-Cylindrica), *Agr Biol Chem Tokyo*, 1990, **54**, 2967-2978.
6. H. Demir, A. Top, D. Balkose and S. Ulku, Dye adsorption behavior of Luffa cylindrica fibers, *J Hazard Mater*, 2008, **153**, 389-394.
7. M. Ahmadi, F. Vahabzadeh, B. Bonakdarpour and M. Mehranian, Empirical modeling of olive oil mill wastewater treatment using loofa-immobilized Phanerochaete chrysosporium, *Process Biochem*, 2006, **41**, 1148-1154.
8. J. P. Chen and T. C. Lin, Loofa sponge as a scaffold for culture of rat hepatocytes, *Biotechnol Progr*, 2005, **21**, 315-319.

9. G. Siqueira, J. Bras, N. Follain, S. Belbekhouche, S. Marais and A. Dufresne, Thermal and mechanical properties of bio-nanocomposites reinforced by Luffa cylindrica cellulose nanocrystals, *Carbohyd Polym*, 2013, **91**, 711-717.
10. G. C. Papanicolaou, E. Psarra and D. Anastasiou, Manufacturing and mechanical response optimization of epoxy resin/Luffa Cylindrica composite, *J Appl Polym Sci*, 2015, **132**.
11. G. Siqueira, J. Bras and A. Dufresne, Luffa Cylindrica as a Lignocellulosic Source of Fiber, Microfibrillated Cellulose, and Cellulose Nanocrystals, *Bioresources*, 2010, **5**, 727-740.
12. C. A. Boynard and J. R. M. D'Almeida, Water absorption by sponge gourd (luffa cylindrica)-polyester composite materials, *J Mater Sci Lett*, 1999, **18**, 1789-1791.
13. S. Acosta-Rubi, A. T. Campocosio, M. D. Montes-Horcasitas, L. Quintanar-Vera, F. Esparza-Garcia and R. Rodriguez-Vazquez, Production of a halotolerant biofilm from green coffee beans immobilized on loofah fiber (Luffa cylindrica) and its effect on phenanthrene degradation in seawater, *J Environ Sci Heal A*, 2017, **52**, 632-640.
14. S. M. Stella and U. Vijayalakshmi, Influence of chemically modified Luffa on the preparation of nanofiber and its biological evaluation for biomedical applications, *J Biomed Mater Res A*, 2019, **107**, 610-620.
15. P. In-na, A. A. Umar, A. D. Wallace, M. C. Flickinger, G. S. Caldwell and J. G. M. Lee, Loofah-based microalgae and cyanobacteria biocomposites for intensifying carbon dioxide capture, *J Co2 Util*, 2020, **42**.
16. Z. J. Ma, W. B. Chen, Z. L. Hu, X. Z. Pan, M. Y. Peng, G. P. Dong, S. F. Zhou, Q. Y. Zhang, Z. M. Yang and J. R. Qiu, Luffa-Sponge-Like Glass-TiO2 Composite Fibers as Efficient Photocatalysts for Environmental Remediation, *Acs Appl Mater Inter*, 2013, **5**, 7527-7536.
17. P. Yuan, D. Y. Tan and F. Annabi-Bergaya, Properties and applications of halloysite nanotubes: recent research advances and future prospects, *Appl Clay Sci*, 2015, **112**, 75-93.
18. Y. Wu, Y. Z. Zhang, J. P. Ju, H. Yan, X. Y. Huang and Y. Q. Tan, Advances in Halloysite Nanotubes-Polysaccharide Nanocomposite Preparation and Applications, *Polymers-Basel*, 2019, **11**.
19. H. B. Gu, C. T. Liu, J. H. Zhu, J. W. Gu, E. K. Wujcik, L. Shao, N. Wang, H. G. Wei, R. Scaffaro, J. X. Zhang and Z. H. Guo, Introducing advanced composites and hybrid materials, *Adv Compos Hybrid Ma*, 2018, **1**, 1-5.
20. L. Lisuzzo and B. Wicklein, Lo Dico G., Lazzara G., del Real G., Aranda P., Ruiz-Hitzky E. Functional biohybrid materials based on halloysite, sepiolite and cellulose nanofibers for health applications, *Dalton Trans*, 2020, **49**, 3830-3840.
21. G. J. Churchman, T. J. Davy, L. A. G. Aylmore, R. J. Gilkes and P. G. Self, Characteristics of Fine Pores in Some Halloysites, *Clay Miner*, 1995, **30**, 89-98.
22. L. Ai, J. Su, M. Wang and J. Jiang, Bamboo-structured nitrogen-doped carbon nanotube coencapsulating cobalt and molybdenum carbide nanoparticles: an efficient bifunctional electrocatalyst for overall water splitting, *ACS Sustainable Chemistry & Engineering*, 2018, **6**, 9912-9920.
23. H. H. P. Yiu, P. A. Wright and N. P. Botting, Enzyme immobilisation using siliceous mesoporous molecular sieves, *Micropor Mesopor Mat*, 2001, **44**, 763-768.
24. Y. Li, X. Yuan, L. Jiang, H. Dai, Y. Zhao, X. Guan, J. Bai and H. Wang, Manipulation of halloysite clay nanotube lumen for environmental remediation: A review, *Environmental Science: Nano*, 2022.
25. V. Vergaro, E. Abdullayev, Y. M. Lvov, A. Zeitoun, R. Cingolani, R. Rinaldi and S. Leporatti, Cytocompatibility and Uptake of Halloysite Clay Nanotubes, *Biomacromolecules*, 2010, **11**, 820-826.
26. I. Gulcin, Antioxidant properties of resveratrol: A structure-activity insight, *Innov Food Sci Emerg*, 2010, **11**, 210-218.
27. F. Brisdelli, G. D'Andrea and A. Bozzi, Resveratrol: A Natural Polyphenol with Multiple Chemopreventive Properties (Review), *Curr Drug Metab*, 2009, **10**, 530-546.
28. M. Wicinski, A. Domanowska, E. Wodkiewicz and B. Malinowski, Neuroprotective Properties of Resveratrol and Its Derivatives-Influence on Potential Mechanisms Leading to the Development of Alzheimer's Disease, *Int J Mol Sci*, 2020, **21**.
29. A. R. Pedrazzo, F. Caldera, M. Zanetti, S. L. Appleton, N. K. Dahkar and F. Trotta, Mechanochemical green synthesis of hyper-crosslinked cyclodextrin polymers, *Beilstein J Org Chem*, 2020, **16**, 1554-1563.
30. W. T. Liang, C. Yang, D. Y. Zhou, H. Haneoka, M. Nishijima, G. Fukuhara, T. Mori, F. Castiglione, A. Mele, F. Caldera, F. Trotta and Y. Inoue, Phase-controlled supramolecular photochirogenesis in cyclodextrin nanosponges, *Chem Commun*, 2013, **49**, 3510-3512.
31. Y. X. Chen, N. Su, K. T. Zhang, S. L. Zhu, L. Zhao, F. Fang, L. Y. Ren and Y. Guo, In-Depth Analysis of the Structure and Properties of Two Varieties of Natural Luffa Sponge Fibers, *Materials*, 2017, **10**.
32. J. M. Falcon, T. Sawczen and I. V. Aoki, Dodecylamine-Loaded Halloysite Nanocontainers for Active Anticorrosion Coatings, *Front Mater*, 2015, **2**.
33. W. J. Huang, S. Fernando, L. F. Allard and Y. P. Sun, Solubilization of single-walled carbon nanotubes with diamine-terminated oligomeric poly(ethylene glycol) in different functionalization reactions, *Nano Lett*, 2003, **3**, 565-568.
34. C. Liu, K. V. Hong, X. Sun, A. Natan, P. C. Luan, Y. Yang and H. L. Zhu, An 'antifouling' porous loofah sponge with internal microchannels as solar absorbers and water pumpers for thermal desalination, *Journal of Materials Chemistry A*, 2020, **8**, 12323-12333.
35. M. Barman, S. Mahmood, R. Augustine, A. Hasan, S. Thomas and K. Ghosal, Natural halloysite nanotubes/chitosan based bio-nanocomposite for delivering norfloxacin, an anti-microbial agent in sustained release manner, *Int. J. Biol. Macromol.*, 2020, **162**, 1849-1861.
36. J. Choi, H. Lee, B. Sohn, M. Song and S. Jeon, Highly efficient evaporative cooling by all-day water evaporation using hierarchically porous biomass, *Sci Rep-Uk*, 2021, **11**.
37. Y. Yuan, S. G. Zhou, Y. Liu and J. H. Tang, Nanostructured Macroporous Bioanode Based on Polyaniline-Modified Natural Loofah Sponge for High-Performance Microbial Fuel Cells, *Environ Sci Technol*, 2013, **47**, 14525-14532.
38. S. T. Yang, J. Kim and W. S. Ahn, CO2 adsorption over ion-exchanged zeolite beta with alkali and alkaline earth metal ions, *Micropor Mesopor Mat*, 2010, **135**, 90-94.
39. M. R. Delgado and C. O. Arean, Carbon monoxide, dinitrogen and carbon dioxide adsorption on zeolite H-Beta: IR spectroscopic and thermodynamic studies, *Energy*, 2011, **36**, 5286-5291.
40. R. M. Serra, F. S. de Vilhena, L. B. Gutierrez, J. M. S. Junior, G. B. Ferreira, T. C. dos Santos, C. M. Ronconi, J. W. M. de Carneiro and A. V. Boix, Experimental and theoretical investigation of the Na+ -> Li+ cation exchange in mordenite and its effect on CO2 adsorption properties, *Adsorption*, 2021, DOI: 10.1007/s10450-020-00288-3.
41. A. Villarreal, G. Garbarino, P. Riani, E. Finocchio, B. Bosio, J. Ramirez and G. Busca, Adsorption and separation of CO2 from N-2-rich gas on zeolites: Na-X faujasite vs Na-mordenite, *J Co2 Util*, 2017, **19**, 266-275.
42. J. Pires, J. Juzkow and M. L. Pinto, Amino acid modified montmorillonite clays as sustainable materials for carbon dioxide adsorption and separation, *Colloid Surface A*, 2018, **544**, 105-110.

43. U. Kamran and S. J. Park, Acetic acid-mediated cellulose-based carbons: Influence of activation conditions on textural features and carbon dioxide uptakes, *J Colloid Interf Sci*, 2021, **594**, 745-758.
44. F. L. Bernard, R. B. Duczinski, M. F. Rojas, M. C. C. Fialho, L. A. Carreno, V. V. Chaban, F. Dalla Vecchia and S. Einloft, Cellulose based poly(ionic liquids): Tuning cation-anion interaction to improve carbon dioxide sorption, *Fuel*, 2018, **211**, 76-86.
45. R. M. Gong, J. Zhang, J. Zhu, J. T. Wang, Q. M. Lai and B. Jiang, Loofah sponge activated by periodate oxidation as a carrier for covalent immobilization of lipase, *Korean J Chem Eng*, 2013, **30**, 1620-1625.
46. L. Stevens, K. Williams, W. Y. Han, T. Drage, C. Snape, J. Wood and J. W. Wang, Preparation and CO2 adsorption of diamine modified montmorillonite via exfoliation grafting route, *Chem Eng J*, 2013, **215**, 699-708.
47. G. V. N. Edward Gomez-Delgado, Ana Lea Cukierman, Pablo R. Bonelli, Influence of the carbonization atmosphere on the development of highly microporous adsorbents tailored to CO2 capture, *Journal of the Energy Institute*, 2022, **102**, 184-189.
48. J. B. Changdan Ma, Xin Hu, Zhuohan Jiang, Linlin Wang, Nitrogen-doped porous carbons from polyacrylonitrile fiber as effective CO2 adsorbents, *Journal of Environmental Sciences*, 2023, **125**, 533-543.
49. R. Fiorenza, M. Bellardita, S. A. Balsamo, L. Spitaleri, A. Gulino, M. Condorelli, L. D'Urso, S. Scire and L. Palmisano, A solar photothermocatalytic approach for the CO2 conversion: Investigation of different synergisms on CoO-CuO/brookite TiO2-CeO2 catalysts, *Chem Eng J*, 2022, **428**.
50. V. Patamia, D. Gentile, R. Fiorenza, V. Muccilli, P. G. Mineo, S. Scire and A. Rescifina, Nanosponges based on self-assembled starfish-shaped cucurbit[6]urils functionalized with imidazolium arms, *Chem Commun (Camb)*, 2021, **57**, 3664-3667.
51. H. Kim, Y. Kim, M. Yoon, S. Linn, S. M. Park, G. Seo and K. Kim, Highly Selective Carbon Dioxide Sorption in an Organic Molecular Porous Material, *J Am Chem Soc*, 2010, **132**, 12200-12202.
52. A. A. Fisher, Folliculitis from the Use of a Loofah Cosmetic Sponge, *Cutis*, 1994, **54**, 12-13.
53. Y. J. Suh, Use of Natural Halloysite as a Functional Cosmetics Carrier, *Econ Environ Geol*, 2015, **48**, 247-253.
54. E. Markiewicz, J. Jerome, T. Mammone and O. C. Idowu, Anti-Glycation and Anti-Aging Properties of Resveratrol Derivatives in the in-vitro 3D Models of Human Skin, *Clin Cosmet Inv Derm*, 2022, **15**, 911-927.
55. Y. N. Zhao, C. Cai, M. Liu, Y. P. Zhao, Y. S. Wu, Z. P. Fan, Z. Ding, H. Z. Zhang, Z. P. Wang and J. Han, Drug-binding albumins forming stabilized nanoparticles for co-delivery of paclitaxel and resveratrol: In vitro/in vivo evaluation and binding properties investigation, *Int J Biol Macromol*, 2020, **153**, 873-882.
56. K. A. Ansari, P. R. Vavia, F. Trotta and R. Cavalli, Cyclodextrin-Based Nanosponges for Delivery of Resveratrol: In Vitro Characterisation, Stability, Cytotoxicity and Permeation Study, *Aaps Pharmscitech*, 2011, **12**, 279-286.
57. N. Summerlin, E. Soo, S. Thakur, Z. Qu, S. Jambhrunkar and A. Popat, Resveratrol nanoformulations: Challenges and opportunities, *Int J Pharmaceut*, 2015, **479**, 282-290.
58. V. Vergaro, Y. M. Lvov and S. Leporatti, Halloysite Clay Nanotubes for Resveratrol Delivery to Cancer Cells, *Macromol Biosci*, 2012, **12**, 1265-1271.
59. J. Chen, N. Wei, M. Lopez-Garcia, D. Ambrose, J. Lee, C. Annelin and T. Peterson, Development and evaluation of resveratrol, Vitamin E, and epigallocatechin gallate loaded lipid nanoparticles for skin care applications, *Eur J Pharm Biopharm*, 2017, **117**, 286-291.
60. C. Cernigliaro, A. D'Anneo, D. Carlisi, M. Giuliano, A. M. Gammazza, R. Barone, L. Longhitano, F. Cappello, S. Emanuele, A. Distefano, C. Campanella, G. Calvaruso and M. Lauricella, Ethanol-Mediated Stress Promotes Autophagic Survival and Aggressiveness of Colon Cancer Cells via Activation of Nrf2/HO-1 Pathway, *Cancers*, 2019, **11**.